Stress-induced martensitic transformation of $Cu_{50}Zr_{50}$ shape memory alloy optimized through microalloying and co-microalloying

F. De Luca[a], P. Nnamchi[b], A. Younes[b], A. T. Fry[a], S. González[b,*]

[a] National Physical Laboratory, Hampton Road, Teddington, Middlesex, TW11 0LW, UK

[b] Faculty of Engineering and Environment, Northumbria University, Newcastle upon Tyne NE1 8ST, UK

Abstract

The stress-induced martensitic transformation of $Cu_{50}Zr_{50}$ at. % shape memory alloy was tuned through microalloying and co-microalloying. The effect of microalloying elements Co or Ni individually or combined (i.e., co-microalloying) was investigated and compared at the macro- and nanoscale. From nanoindentation experiments, change in the slopes of (P/h)-h curves, plastic index and recovery ratio after annealing were investigated: partial replacement of Cu by 1 at. % Ni was observed to promote twinning while for 1 at. % Co the twinning propensity decreased and co-microalloying using 0.5 at. % Co and Ni had an intermediate effect. The recovery ratio of the $Cu_{50}Zr_{50}$ alloy, calculated from the volume change of a residual indent after annealing at 400 ˚C for 5 min after annealing at 400°C for 5 min increased from 15.6 % to 19.5 % when substituting Cu by 1 at. % Ni. These results, obtained at the nanoscale, are in agreement with macroscale test observation, namely, differential scanning calorimetry and x-ray diffraction. Therefore, microalloying opens up possibilities for the development of more cost-effective CuZr alloys, with a view to develop commercial actuators that could replace costly NiTi alloys in the near future.

Keywords: Shape memory alloy; Microalloying; Co-microalloying; Martensitic transformation

1. Introduction

Over the past few years, different types of Shape Memory Alloys (SMAs) have been developed, such as near equiatomic Ni-Ti alloys, which exhibit the best performance with shape recovery up to 7% [1]. However, the high cost associated with expensive Ti element has led to an increasing interest in replacing Ni-Ti alloys by lower cost SMAs.

New SMAs, Fe-based [2] and Cu-based [3] have been reported to exhibit superelastic strain that largely surpasses that of NiTi. Other alloys such as CuZr alloys are promising due to their relatively low cost but they exhibit relatively low performance and this can be improved by tuning the alloy composition [4] through microalloying control i.e., nature and volume fraction of microalloying element [5]. An important drawback of most Cu-based SMAs is the brittleness associated with large grain size [6], although some Cu-based SMAs have their properties optimized when the grain size is rather large [7, 8].

For this reason, it is useful to fabricate fine-grained alloys in order to improve their ductility [9]. A successful method to decrease the grain size is to use rapid solidification techniques. In addition, it enables austenite to retain microalloying elements in solid solution when the cooling rate is high enough, allowing to tune the twinning propensity of austenite grains. A high quenching rate not only prevents segregation of microalloying elements towards grain boundaries, which hinder embrittlement [6], but may also lead to the formation of a partly or fully amorphous phase. Due to the inherent brittleness of amorphous phase, its volume fraction should be minimized to prevent catastrophic failure. An efficient method to improve the ductility of metallic glasses is to promote the formation of crystalline phases embedded in the amorphous phase, i.e., metallic glass composite, especially when the phase is austenite. The later has the propensity to transform into martensite upon loading, promoting work-hardening and, therefore, delaying necking [10]. The propensity can be tuned through accurate control of the nature and concentration of microalloying element/s [4]. Among them, Co and Ni were reported to be some of the most efficient elements in decreasing the stacking fault energy of B2-CuZr austenite, i.e., they promote twinning, at relative low cost compared to Ti. However, the previous studies were only done for limited compositions (i.e., partial substitution of only 0.5 at. % Cu atoms from B2 phase) [4, 11]. Although some authors have studied the effect of alloying on the microstructural and mechanical performance of the CuZr-based system [12-15], the number of studies investigating the use of microalloying as a strategy to tune the twinning propensity of B2-CuZr phase is very scarce [5, 16], with an emphasis on nanoindentation [17-19]. However, the effect of co-microalloying on the twinning propensity has not been explored yet.

This work aims to explore the effect of microalloying and co-microalloying using Co and Ni as potential elements to promote the twinning propensity of CuZr shape memory alloys, using concentrations never explored before. Our results, obtained from the nano- and macro-scale, confirm that microalloying and co-microalloying represent a great potential as a strategy to fine tune the performance of shape memory materials for microelectromechanical systems (MEMS) applications.

2. Methods

Alloy ingots with nominal composition of $Cu_{50}Zr_{50}$, $Cu_{49}Zr_{50}Co_{1,}$ $Cu_{49}Zr_{50}Ni_{1}$ and $Cu_{49}Zr_{50}Co_{0.5}Ni_{0.5}$ at. % were prepared from elements with purity of at least 99.9 at %. The master alloys were re-melted three times in a Ti-gettered high purity argon atmosphere to attain chemical homogeneity. Rod samples with a diameter of 4 mm were obtained from the master alloy by copper mould casting in an inert gas atmosphere. The structure of the as-cast and pre-compressed samples (at a force of19.2 KN, held for 5 min) was studied by X-ray diffraction (XRD), using a Bruker D8 diffractometer with monochromated Cu-Kα radiation (2θ =[20°-90°],

step size = 0.03°). Thermal behaviour of the samples were studied using differential scanning calorimetry (DSC, SETARAM C131 EVO), using a heating and cooling rate of 5 °C/min up to 400 °C and 40 °C/min down to room temperature, respectively. The microstructure was investigated by scanning electron microscopy (SEM) (Zeiss Supra 55-VP) equipped with energy dispersive X-ray (EDX) analysis. Nanoindentation were performed with a high temperature vacuum nanoindentation system (NanoTest Xtreme, Micro Materials, UK). Indents were made in ambient conditions at a loading rate of 50 $\mu N.s^{-1}$ and a maximum load of 1 mN, using a diamond Berkovich indenter. To get an average and representative value, at least 5 valid indents (contained within the phase of interest) were made per composition on individual B2-CuZr austenite grains. As a result of sample quenching, the austenite grains exhibit a dendritic shape. SEM observation and selection of large dendrites allowed for identification of suitable location to carry out indentation. In order to confine the plastic field generated by the indenter within the austenite phase, indents were made in portion of dendrites wider than 1 µm, at least 20 times the maximum depth reached during indentation.

The shape memory behaviour of the different samples was assessed by means of recovery ratio (RR: ability of a material to recover permanent strains), measuring indent change of depth upon annealing at 400 ˚C for 5 min. Prior to annealing the sample were indented to a load of 8 mN, at a loading rate of 400 $\mu N.s^{-1}$. The residual indent depth after indentation, and prior to annealing ($h_{ind\text{-}b}$), was measured by acquiring a 3D topographic scan (5 by 5 µm) of the sample surface, using the same Berkovich tip, at a load of 1 µN and a resolution step of 30 nm. Annealing of the samples was also conducted within the indenter chamber under vacuum (10^{-7} mbar, $[O_2] = 2.5 .10^{-3}$ ppm), without moving the relative position and orientation of the sample to the indenter. The sample was heated to 400˚C using the hot stage of the high temperature indenter, controlling the temperature of the sample with a thermocouple mounted on its surface. The residual indent depth after annealing ($h_{ind\text{-}a}$) was measured following the same scanning procedure, at room temperature. The recovery ratio (RR) was defined as:

$$RR\ (\%) = \frac{h_{ind-b} - h_{ind-a}}{h_{ind-b}} \cdot 100 \qquad (5)$$

where $h_{ind\text{-}b}$ and $h_{ind\text{-}a}$ are the depth of the indent marks before and after heating, respectively.

3. Results and discussion

The mechanical behaviour of the studied alloys (i.e., $Cu_{50}Zr_{50}$, $Cu_{49}Zr_{50}Co_{1,}$ $Cu_{49}Zr_{50}Ni_1$ and $Cu_{49}Zr_{50}Co_{0.5}Ni_{0.5}$ at. %) were investigated by means of 5 to 10 nanoindentation, performed on different austenite dendrites [17-19]. The size of the indents was about 500 nm wide, much

smaller than the dendrite size, as shown in the representative SEM micrograph of an indented austenite dendrite presented in Fig. 1. In order to prevent any influence of the grain boundaries and surrounding amorphous phase, indents fully contained within the dendrite and at least 500 nm away from the nearest edge of the dendrite (maximum depth of 50 nm, at 1 mN) were considered valid. Fig. 2a, c, e and g shows the load-displacement (*P-h*) curves obtained from the indentation of the austenite dendrites of $Cu_{50}Zr_{50}$, $Cu_{49}Zr_{50}Ni_{1,}$ $Cu_{49}Zr_{50}Co_{0.5}Ni_{0.5}$ and $Cu_{49}Zr_{50}Co_1$ at. %, respectively. These results are the most representative from the statistical study of multiple nanoindentations performed on each sample. The curves show the presence of displacement bursts, called pop-ins, starting at a very early stage of the loading segment, as highlighted by arrows on the (P-h) curve. In addition, the slopes of the (P/h)-h plots for $Cu_{50}Zr_{50}$ (Fig. 2b), $Cu_{49}Zr_{50}Ni_1$ (Fig. 2d), $Cu_{49}Zr_{50}Co_{0.5}Ni_{0.5}$ (Fig. 2f) and $Cu_{49}Zr_{50}Ni_1$ (Fig. 2h) at. % were calculated from Fig. 2a, c, e and g, respectively. Although the slopes are different for each composition, they all follow a similar trend; at an early stage, prior to the first pop-in, the slope is low and rapidly steepens as P/h increases. For $Cu_{50}Zr_{50}$, the slopes of the (P/h)-h curve increase from 0.48 to 1.07 $\mu N.nm^{-2}$, past the second pop-in. The largest slope increase, after the second pop-in, was observed for the alloy containing 1 at. % Ni, with a rise from about 0.27 to 1.24 $\mu N.nm^{-2}$. On the other hand, the alloy containing 1 at. % Co exhibits an increase in slope from 0.09 to 0.44 $\mu N.nm^{-2}$, with a second slope lower than that of the $Cu_{50}Zr_{50}$ parent alloy. For the co-microalloying composition of $Cu_{49}Zr_{50}Co_{0.5}Ni_{0.5}$, the slope increases from 0.25 to 0.88 $\mu N.nm^{-2}$, with the second slope ranging between that of $Cu_{49}Zr_{50}Ni_1$ and $Cu_{49}Zr_{50}Co_1$. The change in slope, from the first to second pop-in, arises from the change in predominant deformation mode, namely, from dislocation slip to martensitic transformation [18], in agreement with other studies on shape memory materials ~~including TRIP steel~~ such as Fe-28Mn-6Si-5Cr alloy [18]. ~~The value of the second slope for medium-Mn TRIP steel (i.e., 0.535) is similar to that of the alloy containing 1 at. % of Co, but smaller than for the other compositions, especially $Cu_{50}Zr_{50}$ (1.07) and $Cu_{49}Zr_{50}Ni_1$ at % (1.24). The later observation suggests that CuZr alloys exhibit a more efficient martensitic transformation than medium-Mn TRIP steel.~~ Since martensite is harder than austenite, higher (P/h)-h slope relates to more effective martensitic transformation [20]. In other words, alloys undergoing martensitic transformation are more prone to work-hardening. The improvement in the stress-induced martensitic transformation of alloys, where 1 at. % of Cu in B2-CuZr structure have been replaced by either Ni (microalloying) or Ni and Co (co-microalloying), can be attributed to the reduction in the Stacking Fault Energy (SFE) [4]. However, the substitution of Cu by solely Co appears to decrease the propensity of the transformation since (P/h)-h slope is lower than for $Cu_{50}Zr_{50}$ at. % alloy.

The first and second pop-in events provide relevant information regarding the deformation mode occurring at the early stage of plasticity. Hence, the relationship between the critical load, P_c, and the corresponding excursion depth, Δh, at the first pop-in (P_{c1}-Δh_1) and second pop-in

(P_{c2}-Δh_2), was studied for all the different compositions (Fig. 3a and Fig. 3b, respectively). The first pop-in event can be associated to the transition in deformation mode from purely elastic to elastic-plastic (shift from the Hertzian solution, presented in Figure 2), with plasticity occurring through dislocation slip. At higher load, the second pop-in highlight further change in the deformation mode, namely from dislocation slip to martensitic transformation. At the first pop-in (Fig. 3a), the maximum excursion depth for all alloy compositions is smaller than 3 μm, similar to that of Fe-28Mn-6Si-5Cr alloy [18]. The slope of the parent $Cu_{50}Zr_{50}$ alloy was measured about 2.32 and increased to about 10.28 for $Cu_{49}Zr_{50}Ni_1$ alloy due to the substitution of 1 % at of Cu by Ni microalloying element. On the other hand, the use of Co as microalloying element was found to decrease the slope to about 1.52. For the co-microalloying $Cu_{49}Zr_{50}Ni_{0.5}Co_{0.5}$ alloy, the slope was measured about 4.36, ranging between that of $Cu_{49}Zr_{50}Co_1$ and $Cu_{49}Zr_{50}Ni_1$ (Fig. 3a). Differences in slope among the different alloy compositions (Fig. 3a) can be attributed to their different stacking fault energy (SFE). Higher SFE involves smaller dislocation core size and, therefore, dislocations can come closer to each other, enabling a larger accumulated number of dislocations in each slip plane [21]. Lower SFE results in larger dislocation core size, making dislocations less mobile and, therefore, a limited number of dislocations can be accumulated on a slip plane. The excursion depth at the first pop-in event, can be linked to the magnitude of the Burgers vector, |**b**|, through the following equation [18]:

$$\Delta h = n|\mathbf{b}| \qquad (1)$$

where n is the number of geometrically necessary dislocations, linearly proportional to the displacement of the pop-in event. According to Eq. 1 and Fig. 3a, compositions with higher $\frac{dP_{c1}}{d\Delta h_1}$ values than the parent alloy, i.e. $Cu_{49}Zr_{50}Ni_1$ and $Cu_{49}Zr_{50}Co_{0.5}Ni_{0.5}$, are those for which microalloying has decreased the SFE and, therefore, lowered the number of dislocations in a slip plane. On the other hand, the incorporation of 1 at % Co micro-alloying elements in $Cu_{49}Zr_{50}Co_1$ appears to have increased the SFE, leading to a greater number of dislocations in slip plane. Differences in slope among the four compositions (Fig. 3a) can be indirectly attributed to their different stacking fault energy (SFE).

Fig. 3b shows the relationship between the critical load, P_{c2}, and the excursion depth, Δh_2, for the second pop-in. These pop-in events occur when the stress-induced martensite reaches a critical size, larger than the contact area between the indenter tip and sample [22].

The length of the excursion depth of the second pop-ins (Δh_2) is proportional to the thickness increase of twinned martensite plate (Δth), as described in the following equation [22]:

$$\Delta h_2 \sim 0.12\ \Delta \text{th} \qquad (2)$$

According to Eq. 2 and Fig. 3b, for the same thickness increase of twinned martensite, the critical load P_{c2} for the alloys containing 1 at. % Ni and 0.5Co0.5Ni at. % is higher and therefore the slope $\frac{dP_{c2}}{d\Delta h_2}$ is higher than for the parent alloy and the alloy containing 1 at. % Co. The slope increases from about 9.52 for the parent $Cu_{50}Zr_{50}$ at. % alloy to about 10.48 for $Cu_{49}Zr_{50}Ni_1$ at. % while that of $Cu_{49}Zr_{50}Co_1$ at. % decreased to 9.66, indicating that the stress-induced martensitic transformation is best promoted with 1 at. % of Ni micro-alloying element.

In order to assess the influence of microalloying elements on the relative plastic/elastic deformation behaviour of B2-austenite, the plastic index, ζ, was measured for all compositions [23] as follow:

$$\zeta = \frac{A_1}{(A_1+A_2)} \qquad (3)$$

where A_1 and A_2 are the plastic deformation area and the elastic recovery area under the unloading segment of the P-h curves, respectively. The plastic index of a material can vary from ζ = 0, for a purely elastic behaviour, to ζ = 1 for purely plastic. Additionally, the mechanical properties of a crystalline phase can be correlated to the plastic index through the following equation [24]:

$$\zeta = \frac{E}{H}\left(\frac{\sigma}{R}\right)^{1/2} \qquad (4)$$

where E is the elastic modulus, H the hardness, σ the root-mean square surface roughness and R the average radius of curvature of asperities. Because all the different samples were polished and indented following the exact same procedure, the plastic index can directly be related to the mechanical properties of the crystalline phase. Fig. 4 shows the plastic index for the different alloy compositions. A reduction of plasticity was observed for $Cu_{49}Zr_{50}Ni_1$ as compared to $Cu_{50}Zr_{50}$, with an average measured plastic index of 0.49 and 0.52, respectively. The incorporation of 1 at. % Ni favoured the martensitic transformation upon nanoindentation loading, promoting work hardening. On the other hand, addition of 1 at. % Co led to an increase in the plastic index, to a value of 0.54, result of a less effective martensitic transformation. For the alloy containing Co and Ni, the plastic index is approximately intermediate between that of the alloys containing only Co or Ni. Although, there is no information in the current state of literature about the plastic index of shape memory alloys, including the CuZr systems, the results seem reasonable considering that they are similar to those measured in other metallic alloys [25-27].

The shape memory behaviour was characterized by calculating (see equation 5 in Methods) the recovery ratio (RR) obtained from measuring the value of the deepest point of residual indents (indent depth) before (h_{ind-b}) and after annealing (h_{ind-a}) at 400°C for 5 min. No significant change in surface roughness or oxidation was detected after annealing. Fig. 5 shows the 3D image of residual indents, made at a load of 8 mN, before and after annealing at 400˚C for 5 min in vacuum for$Cu_{50}Zr_{50}$and $Cu_{49}Zr_{50}Co_1$ at. % alloys. These results are summarised in Fig. 5e, where the residual indent depth before and after annealing along with the recovery ratio (%) for the four compositions are presented. At the same 8 mN indent load, the initial residual indent depth ranges from about 60 nm for $Cu_{50}Zr_{50}$ to about 116 for $Cu_{50}Zr_{50}Co_1$ at. %, respectively, but decreases after annealing. From both values and equation 5, a recovery ratio of 15.6 % has been obtained for the $Cu_{50}Zr_{50}$ parent alloy, while a maximum value of 19.5 % is obtained for the alloy with 1 at. % Ni. These results confirm that for the Ni-containing SMA, a larger volume fraction of martensite induced upon loading has transformed into martensite.

For NiTi, which is known to exhibit the best shape memory performance among all alloy systems, the recovery ratio obtained from Vickers tests was measured about 30 % independently of the load applied [28]. As far as the authors are concerned, no information for the shape memory CuZr system has been published. We have shown that despite the relatively poor performance of $Cu_{50}Zr_{50}$ alloy with a recovery ratio of 15.6 %, it can be increased to 19.5 % with only 1 at. % Ni addition. These results are promising and open up the possibility to develop more cost-effective commercial CuZr alloys than traditional costly NiTi alloys.

In order to assess the reliability of the results obtained at the nanoscale and, therefore, confirm whether they are representative of the sample bulk behaviour, the thermal behaviour of the as-cast samples and the microstructural changes upon compression for the different alloy compositions were investigated. The thermal behaviour of the $Cu_{50}Zr_{50}$, $Cu_{49}Zr_{50}Co_1$, $Cu_{49}Zr_{50}Ni_1$ and $Cu_{49}Zr_{50}Co_{0.5}Ni_{0.5}$ at. % samples was studied by running DSC scans heating up to 400°C and cooling down (Fig. 6). The temperatures at which martensite starts and finishes to transform into austenite (A_s and A_f, respectively) upon heating, as well as that at which austenite transforms into martensite (M_s) upon cooling are listed in Table 1. While for $Cu_{50}Zr_{50}$ alloy, A_s, A_f and M_s are 258.3°C, 327.7°C, and 58.3°C, respectively, the addition of 1 at. % of Ni shifts all transformation temperatures to higher values, especially A_f, which increases to 363.8°C. These temperatures are far lower than 400°C, at which the recovery ratio was calculated (Fig. 5), ensuring that the stress-induced martensite can fully transform back into austenite. The increase in A_f was shown to be indicative of the promotion of martensitic transformation, as observed by Zhou et al.[16]. On the other hand, the addition to 1 at. % Co shifts the transformation temperatures to lower values, suggesting a decline in the martensitic transformation [29]. For the composition of $Cu_{49}Zr_{50}Co_{0.5}Ni_{0.5}$ at %, A_s, A_f and M_s were measured about 247.2˚C, 283.3˚C and 62.5˚C, respectively, approximately intermediate to those of $Cu_{49}Zr_{50}Co_1$ and $Cu_{49}Zr_{50}Ni_1$ alloys and

similar to $Cu_{50}Zr_{50}$. Although M_s is usually used to assess the efficiency of the martensitic transformation of an alloy, A_s and A_f do follow a similar trend and, therefore, can be equally used for that purpose [9].

Microstructural changes upon compression of the samples (19.2 KN for 5 min) were investigated by XRD (Fig. 7). The XRD patterns of as-cast (Fig. 7a) and compressed (Fig. 7b) $Cu_{50}Zr_{50}$, $Cu_{49}Zr_{50}Co_{1,}$ $Cu_{49}Zr_{50}Ni_1$ and $Cu_{49}Zr_{50}Co_{0.5}Ni_{0.5}$ at. % samples show the presence of peaks associated to the same crystalline phases, with varying relative intensity, depending on their composition. The phases detected consist of orthorhombic $Cu_{10}Zr_7$ (a = 0.9347 nm, b = 0.9347 nm, c = 1.2675 nm), orthorhombic Cu_8Zr_3 (a = 0.78686 nm, b = 0.81467 nm, c = 0.9977 nm), austenite B2 CuZr (a = 3.2562 nm, b = 3.2562 nm, c = 3.2562 nm) and monoclinic martensite B19' CuZr (a = 0.3237 nm, b = 0.4138 nm, c = 0.5449 nm). The intensity of the peak associated with austenite, at about 39°, decreases while the intensity of the peaks associated with martensite, especially the one at about 27.5°, increase after compression. Therefore, the results suggest that austenite transforms into martensite upon compression. While a reduction in the intensity of the XRD peak associated with martensite, at about 28°, was observed for the alloy containing 1 at. % Co, a significant increase was measured for the alloy containing 1 at. % Ni, in comparison to the $Cu_{50}Zr_{50}$ parent alloy. Regarding the alloy containing 0.5 at. % Co and 0.5 at. % Ni, the intensity was found to be comparable to the parent alloy. It was therefore concluded that Ni promotes martensitic transformation of the parent B2-CuZr phase, while Co obstructs the transformation, at least when incorporated to 1 at. %. In the case of the alloy containing 0.5 at. % Co and 0.5 at. % Ni, the two microalloying elements seemed to have compensating effect on the martensitic transformation. The efficiency of the stress-induced martensitic process seems to be composition-dependent, which is in good agreement with previous observations [5].

It was previously reported that 0.5 at. % Co addition promotes the martensitic transformation of B2-CuZr by decreasing the stacking fault energy of the (011)[100] slip system from 381 $mJ.m^{-2}$ to 75 $mJ.m^{-2}$ [4]. Further addition of Co atoms to about 12.5 and 50 at. % decreased the stacking fault energy to 281 and 75 $mJ\text{-}m^{-2}$, respectively [16]. However, for an intermediate concentration in Co of 1 at. %, the stacking fault energy seems to increase as can be deduced from the decrease in the effectiveness for the stress-induced martensitic transformation as proven from the XRD and DSC results. On the other hand, addition of 1 at. % Ni appears to promote the martensitic transformation of the parent B2-CuZr alloy, which is consistent with the increase of M_s (Fig. 6), as compared to $Cu_{50}Zr_{50}$. Smaller Ni additions (i.e., 0.5 at. %) was also reported to promote the martensitic transformation due to the decrease in the stacking fault energy. However, the value of the stacking fault energy remains higher than for 0.5 at. % of Co, which implies that the martensitic transformation should be less effective [4, 16].

4. Conclusions

The effect of microalloying with Co or Ni individually or combined (i.e., co-microalloying) on the twinning propensity of $Cu_{50}Zr_{50}$ at. % was investigated at the nano- and macroscale level. This enabled to assess the strategy of improving the shape memory performance of CuZr alloys through microalloying and, therefore, to develop cost-effective CuZr SMA actuators that could replace costly Ni-Ti SMAs. Partial replacement of Cu by 1 at. % Ni from the parent $Cu_{50}Zr_{50}$ alloy, enabled to improve the recovery ratio after annealing at 400°C for 5 min, from 15.6 % to 19.5 %. Better twinning propensity of B2-austenite was observed, favouring the formation of martensite. Co-microalloying using equal concentrations of Co and Ni did not have a significant effect on the mechanical and thermal behaviour of $Cu_{50}Zr_{50}$ alloy due to the effect of Co in suppressing the formation of martensite.

This works shows that proper selection of microalloying element/s, in optimum concentration, can promote twinning and, therefore, represent a new strategy to enhance the stress sensitivity in CuZr SMA sensors. This research opens up the possibility to explore novel compositions and concentrations to develop cost-effective CuZr SMAs that can achieve, in the future, similar performance to that of NiTi SMAs.

References

[1] C. Jackson, H. Wagner, R. Wasilewski, Report No. NASA-SP 5110, National Aeronautics and Space Administration (1972).

[2] Y. Tanaka, Y. Himuro, R. Kainuma, Y. Sutou, T. Omori, K. Ishida, Ferrous Polycrystalline Shape-Memory Alloy Showing Huge Superelasticity, Science 327(5972) (2010) 1488-1490.

[3] J.P. Oliveira, Z. Zeng, S. Berveiller, D. Bouscaud, F.M. Braz Fernandes, R.M. Miranda, N. Zhou, Laser welding of Cu-Al-Be shape memory alloys: Microstructure and mechanical properties, Materials & Design 148 (2018) 145-152.

[4] Y. Wu, D.Q. Zhou, W.L. Song, H. Wang, Z.Y. Zhang, D. Ma, X.L. Wang, Z.P. Lu, Ductilizing Bulk Metallic Glass Composite by Tailoring Stacking Fault Energy, Physical Review Letters 109(24) (2012) 245506-1-245506-12.

[5] S. González, P. Pérez, E. Rossinyol , S. Surinach, M.D. Baró, E. Pellicer, J. Sort, Drastic influence of minor Fe or Co additions on the glass forming ability, martensitic transformations and mechanical properties of shape memory Zr–Cu–Al bulk metallic glass composites, Science and Technology of Advanced Materials 15(3) (2014) 035015.

[6] T. Tadaki, Shape memory materials, Cambridge University Press, Cambridge; New York, 1998.

[7] Y. Sutou, T. Omori, K. Yamauchi, N. Ono, R. Kainuma, K. Ishida, Effect of grain size and texture on pseudoelasticity in Cu–Al–Mn-based shape memory wire, Acta Materialia 53(15) (2005) 4121-4133.

[8] J.P. Oliveira, Z. Zeng, T. Omori, N. Zhou, R.M. Miranda, F.M.B. Fernandes, Improvement of damping properties in laser processed superelastic Cu-Al-Mn shape memory alloys, Materials & Design 98 (2016) 280-284.

[9] T.W. Duerig, K.N. Melton, D. Stockel, C.M. Wayman, Engineering aspects of shape memory alloys, 1st ed., Butterworth-Heinemann, London, 1990.

[10] S. Pauly, S. Gorantla, G. Wang, U. Kühn, J. Eckert, Transformation-mediated ductility in CuZr-based bulk metallic glasses, Nature materials 9(6) (2010) 473-477.

[11] V.M. Villapún, J. Medina, P. Pérez, F. Esat, F. Inam, S. González, Strategy for preventing excessive wear rate at high loads in bulk metallic glass composites, Materials & Design 135 (2017) 300-308.
[12] K.K. Song, D.Y. Wu, S. Pauly, C.X. Peng, L. Wang, J. Eckert, Thermal stability of B2 CuZr phase, microstructural evolution and martensitic transformation in Cu–Zr–Ti alloys, Intermetallics 67 (2015) 177-184.
[13] D. Wu, K. Song, C. Cao, R. Li, G. Wang, Y. Wu, F. Wan, F. Ding, Y. Shi, X. Bai, I. Kaban, J. Eckert, Deformation-Induced Martensitic Transformation in Cu-Zr-Zn Bulk Metallic Glass Composites, Metals 5(4) (2015) 2134-2147.
[14] G. Yi, X. Zhang, J. Qin, J. Ning, S. Zhang, M. Ma, R. Liu, Effects of Ni and Ti on the phase stability, martensitic transformation and mechanical properties of B2 CuZr phase, Computational Materials Science 110 (2015) 121-125.
[15] Y. Wei, J. Du, R. Chen, Martensitic transformation induced plasticity in ZrCuAl metallic glass composites: Precipitate size and volume effects, Intermetallics 68 (2016) 1-4.
[16] D.Q. Zhou, Y. Wu, H. Wang, X.D. Hui, X.J. Liu, Z.P. Lu, Alloying effects on mechanical properties of the Cu–Zr–Al bulk metallic glass composites, Computational Materials Science 79 (2013) 187-192.
[17] B.B. He, M.X. Huang, Z.Y. Liang, A.H.W. Ngan, H.W. Luo, J. Shi, W.Q. Cao, H. Dong, Nanoindentation investigation on the mechanical stability of individual austenite grains in a medium-Mn transformation-induced plasticity steel, Scripta Materialia 69(3) (2013) 215-218.
[18] K. Sekido, T. Ohmura, T. Sawaguchi, M. Koyama, H.W. Park, K. Tsuzaki, Nanoindentation/atomic force microscopy analyses of ε-martensitic transformation and shape memory effect in Fe–28Mn–6Si–5Cr alloy, Scripta Materialia 65(11) (2011) 942-945.
[19] T.H. Ahn, C.S. Oh, D.H. Kim, K.H. Oh, H. Bei, E.P. George, H.N. Han, Investigation of strain-induced martensitic transformation in metastable austenite using nanoindentation, Scripta Materialia 63(5) (2010) 540-543.
[20] J. Fornell, M.D. Baró, S. Suriñach, A. Gebert, J. Sort, The Influence of Deformation-Induced Martensitic Transformations on the Mechanical Properties of Nanocomposite Cu-Zr-(Al) Systems, Advanced Engineering Materials 13(1-2) (2011) 57-63.
[21] A.A. Kaya, 2 - Physical metallurgy of magnesium, in: M.O. Pekguleryuz, K.U. Kainer, A. Arslan Kaya (Eds.), Fundamentals of Magnesium Alloy Metallurgy, Woodhead Publishing2013, pp. 33-84.
[22] G. Laplanche, J. Pfetzing-Micklich, G. Eggeler, Sudden stress-induced transformation events during nanoindentation of NiTi shape memory alloys, Acta Materialia 78 (2014) 144-160.
[23] J.-y. Sun, J. Tong, Fracture toughness properties of three different biomaterials measured by nanoindentation, Journal of Bionic Engineering 4(1) (2007) 11-17.
[24] Y.-w. Chung, Introduction to materials science and engineering, CRC/Taylor & Francis, Boca Raton, 2007.
[25] B.D. Beake, G.S. Fox-Rabinovich, S.C. Veldhuis, S.R. Goodes, Coating optimisation for high speed machining with advanced nanomechanical test methods, Surface and Coatings Technology 203(13) (2009) 1919-1925.
[26] G. Fox-Rabinovich, S. Veldhuis, G. Dosbaeva, K. Yamamoto, A. Kovalev, D. Wainstein, I. Gershman, L. Shuster, B. Beake, Nanocrystalline coating design for extreme applications based on the concept of complex adaptive behavior, Journal of Applied Physics 103(8) (2008) 083510.
[27] S. Zhang, Nanostructured thin films and coatings, CRC Press, Boca Raton, 2010.
[28] W. Ni, Y.-T. Cheng, D.S. Grummon, Recovery of microindents in a nickel–titanium shape-memory alloy: a “self-healing” effect, Applied physics letters 80(18) (2002) 3310-3312.
[29] C.A. Biffi, M. Coduri, A. Tuissi, CuZr Based Shape Memory Alloys: Effect of Co on the Martensitic Transformation and the Microstructure, Materials Today: Proceedings 2 (2015) S797-S800.

Acknowledgements

This work has been partially financed by EPSRC (EP/P019889/1) First Grant scheme and EMPIR 14IND03 Strength-ABLE Grant. P.N. acknowledges research contract from EPSRC. A. Younes acknowledge research support from Northumbria University.

Data availability

The raw/processed data required to reproduce these findings cannot be shared at this time due to technical or time limitations

Additional information

The authors declare no competing interests

Figure captions

Figure 1. SEM micrograph of a dendrite indented with a grid of indents (14x22 – spacing of 2 µm) - $Cu_{49}Zr_{50}Co_{0.5}Ni_{0.5}$ alloy.

Figure 2. Load-displacement (P-h) curves obtained from indentation in the austenitic phase of CuZr alloys with varying composition (A, C, E and G) and the associated (P/h)-h curves (B, D, F and H). For each composition, an Hertzian solution was fitted to the (P-h) curves (dashed lined).

Figure 3. Relationship between the critical load P_c and the excursion depth Δh for the first and second pop-in (A and B, respectively).

Figure 4. Plasticity index of the alloys compositions extracted from indentation at 1 mN load, in ambient conditions.

Figure 5. 3D image of residual indents, made at 8 mN, for $Cu_{50}Zr_{50}$ and $Cu_{49}Zr_{50}Co_1$ before (A and C, respectively) and after annealing (B and D, respectively) at 400 ˚C for 5 min in vacuum. e) Graph plotting the residual indent depth and recovery ratio (%) for the four compositions.

Figure 6. DSC scans at 20 °C/min for the CuZr alloys of different composition – heating and cooling scans.

Figure 7. XRD diagrams of the different alloy compositions, a) before and b) after compression.

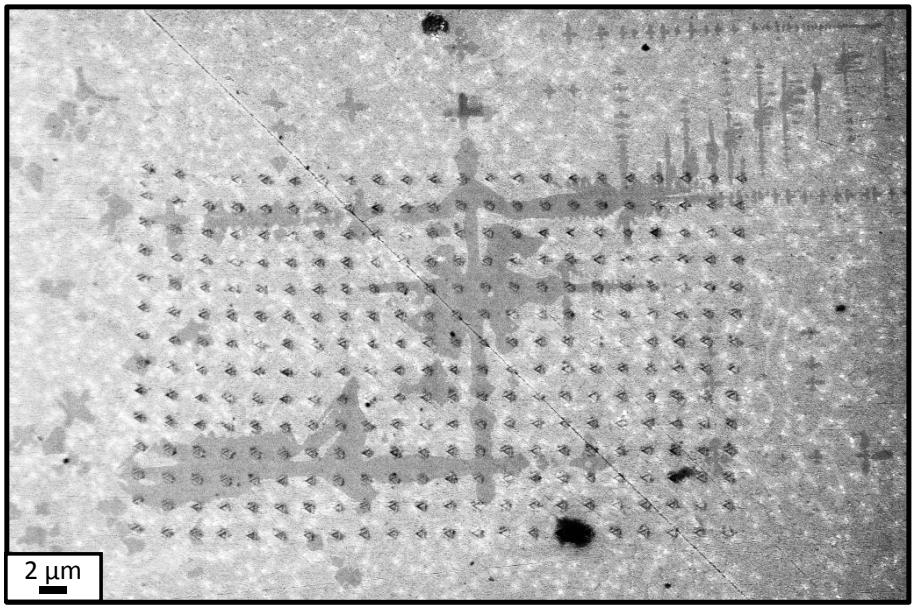

Fig. 1

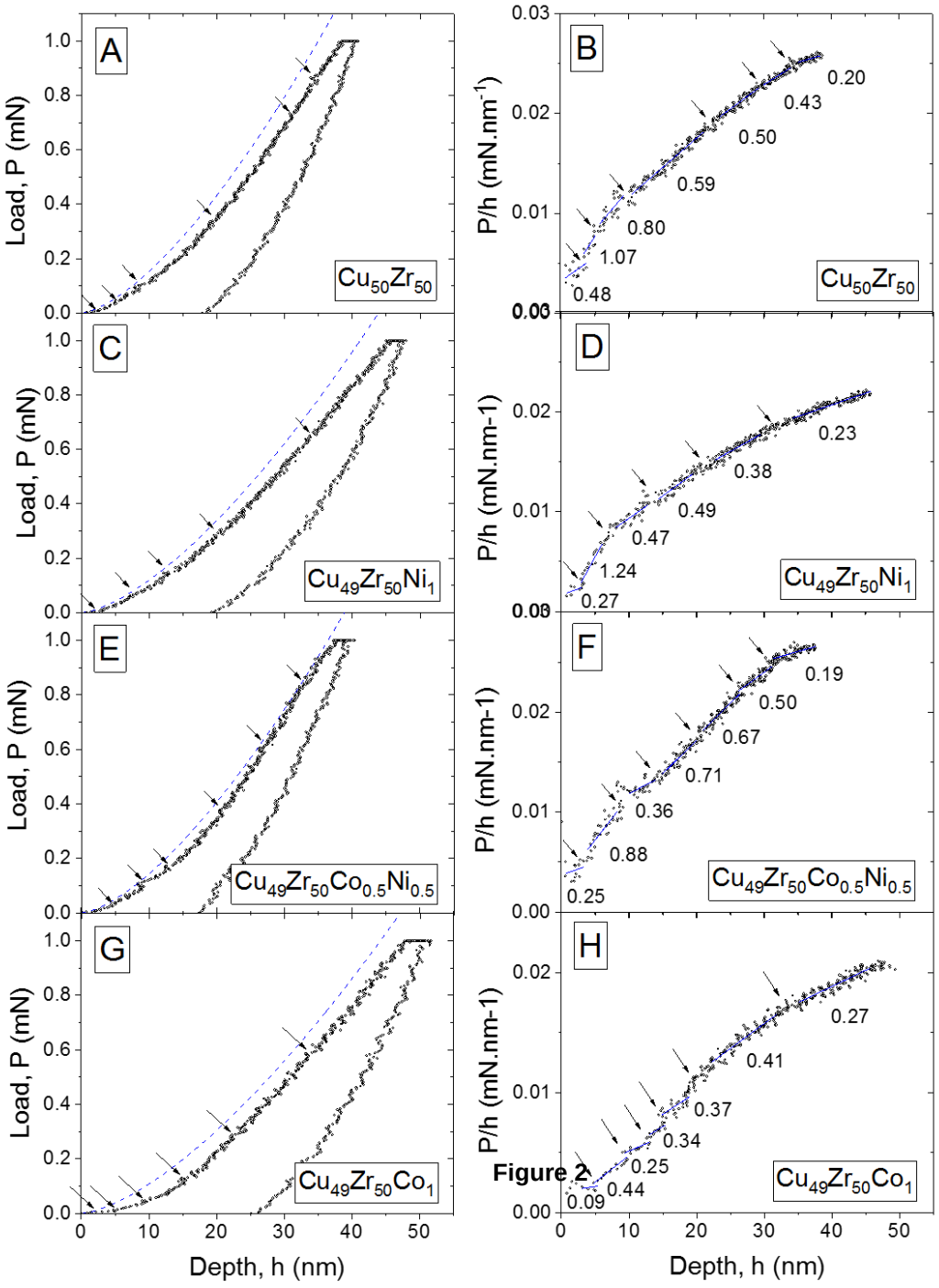
A
B
C
D
E
F
G
H
Load, P (mN)
P/h (mN.nm-1)
Depth, h (nm)
Cu50Zr50
Cu49Zr50Ni1
Cu49Zr50Co0.5Ni0.5
Cu49Zr50Co1
0.48
0.80
1.07
0.59
0.50
0.43
0.20
0.27
1.24
0.47
0.49
0.38
0.23
0.25
0.88
0.36
0.71
0.67
0.50
0.19
0.09
0.44
0.25
0.34
0.37
0.41
0.27

Figure 2

Fig. 2

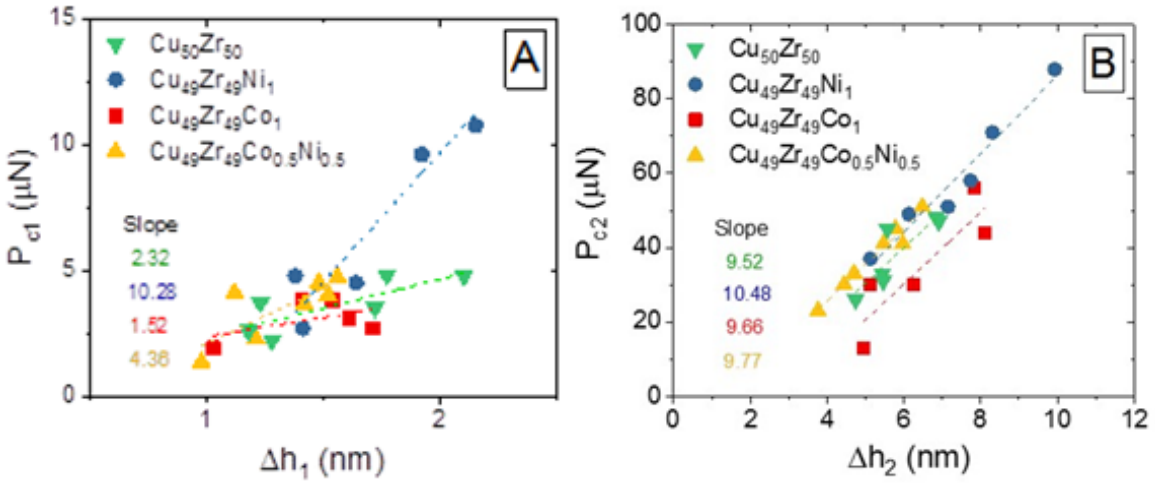
A
B
$Cu_{50}Zr_{50}$
$Cu_{49}Zr_{49}Ni_1$
$Cu_{49}Zr_{49}Co_1$
$Cu_{49}Zr_{49}Co_{0.5}Ni_{0.5}$
Slope
2.32
10.28
1.52
4.36
9.52
10.48
9.66
9.77
P_{c1} (μN)
P_{c2} (μN)
Δh_1 (nm)
Δh_2 (nm)

Fig. 3

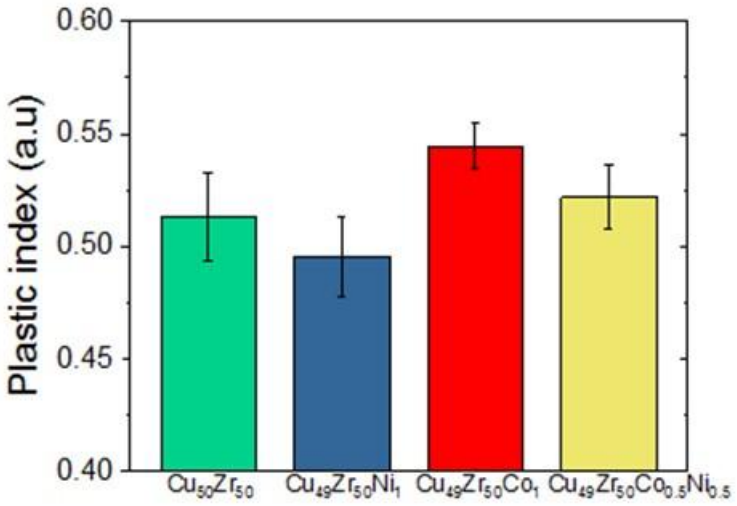
Plastic index (a.u)
0.60
0.55
0.50
0.45
0.40
Cu50Zr50
Cu49Zr50Ni1
Cu49Zr50Co1
Cu49Zr50Co0.5Ni0.5

Fig. 4

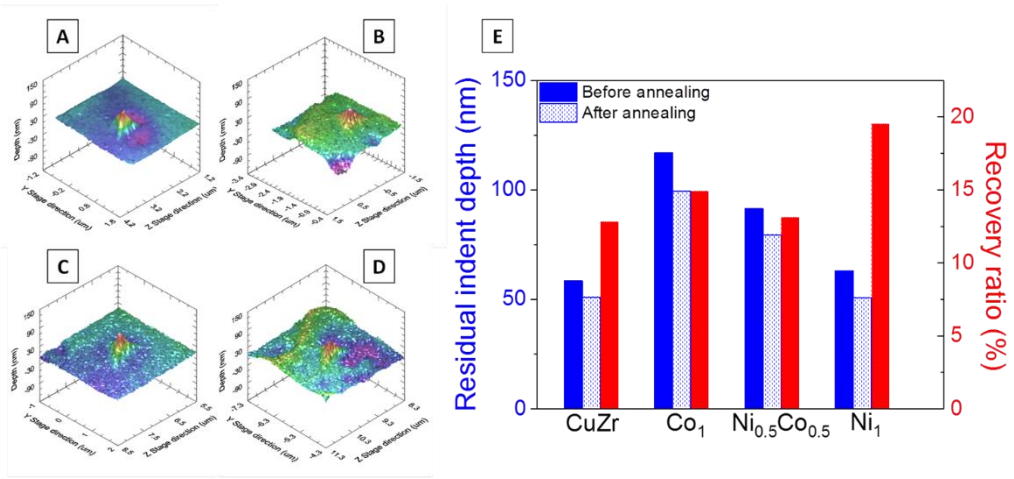
A
B
C
D
E
Before annealing
After annealing
Residual indent depth (nm)
Recovery ratio (%)
150
100
50
0
20
15
10
5
0
CuZr
Co1
Ni0.5Co0.5
Ni1

Fig. 5

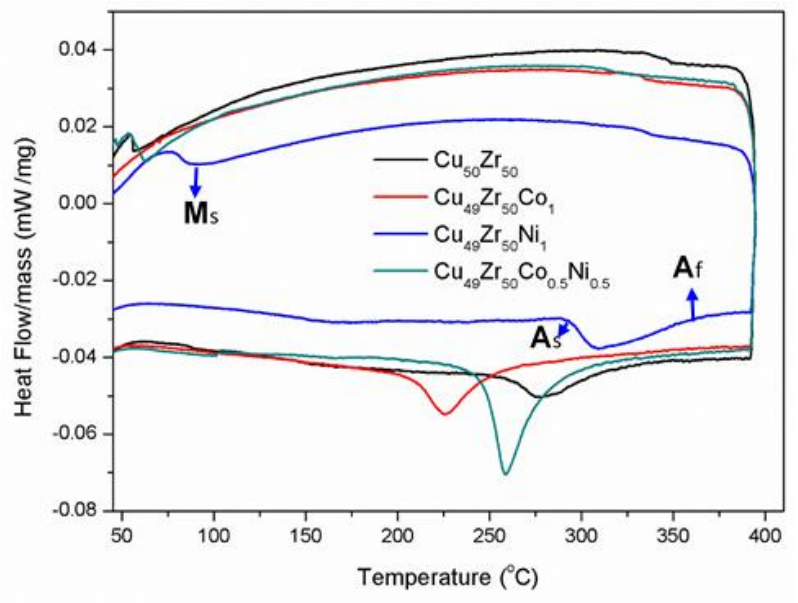
0.04
0.02
0.00
-0.02
-0.04
-0.06
-0.08
50
100
150
200
250
300
350
400
Heat Flow/mass (mW /mg)
Temperature (°C)
Cu50Zr50
Cu49Zr50Co1
Cu49Zr50Ni1
Cu49Zr50Co0.5Ni0.5
Ms
As
Af

Fig. 6

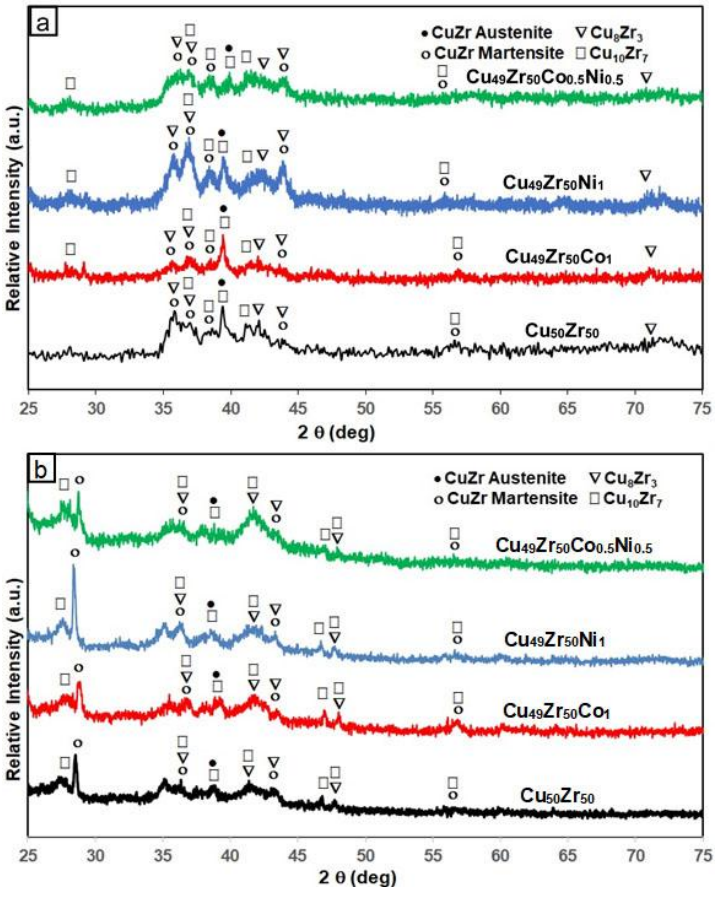
a
• CuZr Austenite ▽ Cu_8Zr_3
o CuZr Martensite □ $Cu_{10}Zr_7$
$Cu_{49}Zr_{50}Co_{0.5}Ni_{0.5}$
$Cu_{49}Zr_{50}Ni_1$
$Cu_{49}Zr_{50}Co_1$
$Cu_{50}Zr_{50}$
Relative Intensity (a.u.)
25 30 35 40 45 50 55 60 65 70 75
2 θ (deg)
b
• CuZr Austenite ▽ Cu_8Zr_3
o CuZr Martensite □ $Cu_{10}Zr_7$
$Cu_{49}Zr_{50}Co_{0.5}Ni_{0.5}$
$Cu_{49}Zr_{50}Ni_1$
$Cu_{49}Zr_{50}Co_1$
$Cu_{50}Zr_{50}$
Relative Intensity (a.u.)
25 30 35 40 45 50 55 60 65 70 75
2 θ (deg)

Fig. 7

Table 1

Composition (at. %)	A_s (°C)	A_f (°C)	M_s (°C)
$Cu_{50}Zr_{50}$	258.3	327.7	58.3
$Cu_{49}Zr_{50}Co_1$	211.1	252.8	<40
$Cu_{49}Zr_{50}Ni_1$	291.7	363.8	88.8
$Cu_{49}Zr_{50}Co_{0.5}Ni_{0.5}$	247.2	283.3	62.5

Graphical Abstract (for review)

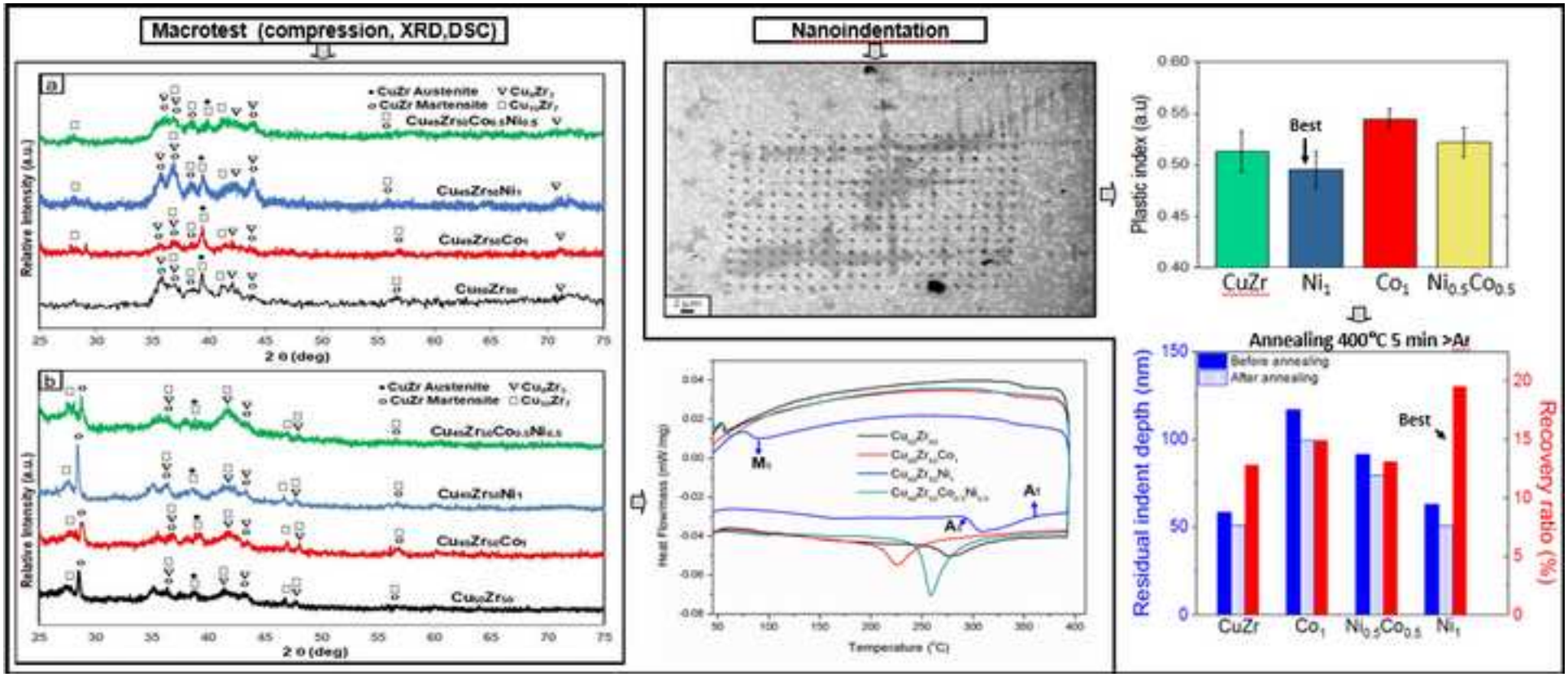

Highlights

- Partial replacement of Cu by 1 at. % Ni in $Cu_{50}Zr_{50}$ at. % alloy was observed to promote twinning.
- The twinning propensity decreases for 1 at. % Co and it is intermediate for 0.5 at. % Co and Ni.
- The results at nanoscale are in agreement with macroscale test observations.
- Microalloying opens up possibilities for the development of more cost-effective CuZr alloys.

Table

Table 1

Composition (at. %)	A_s (°C)	A_f (°C)	M_s (°C)
$Cu_{50}Zr_{50}$	258.3	327.7	58.3
$Cu_{49}Zr_{50}Co_1$	211.1	252.8	<40
$Cu_{49}Zr_{50}Ni_1$	291.7	363.8	88.8
$Cu_{49}Zr_{50}Co_{0.5}Ni_{0.5}$	247.2	283.3	62.5

Figure

Click here to download high resolution image

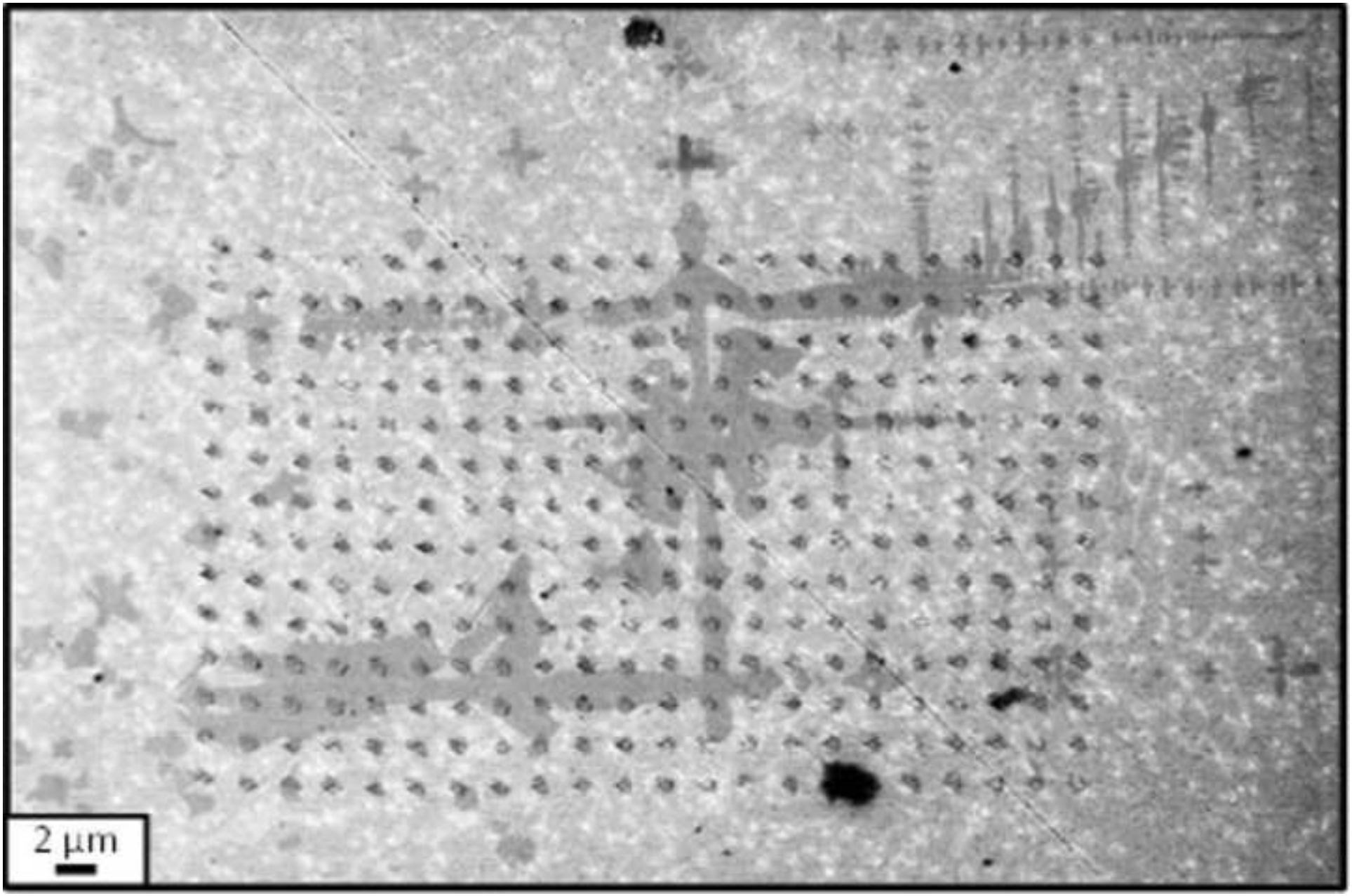

Figure

Click here to download high resolution image

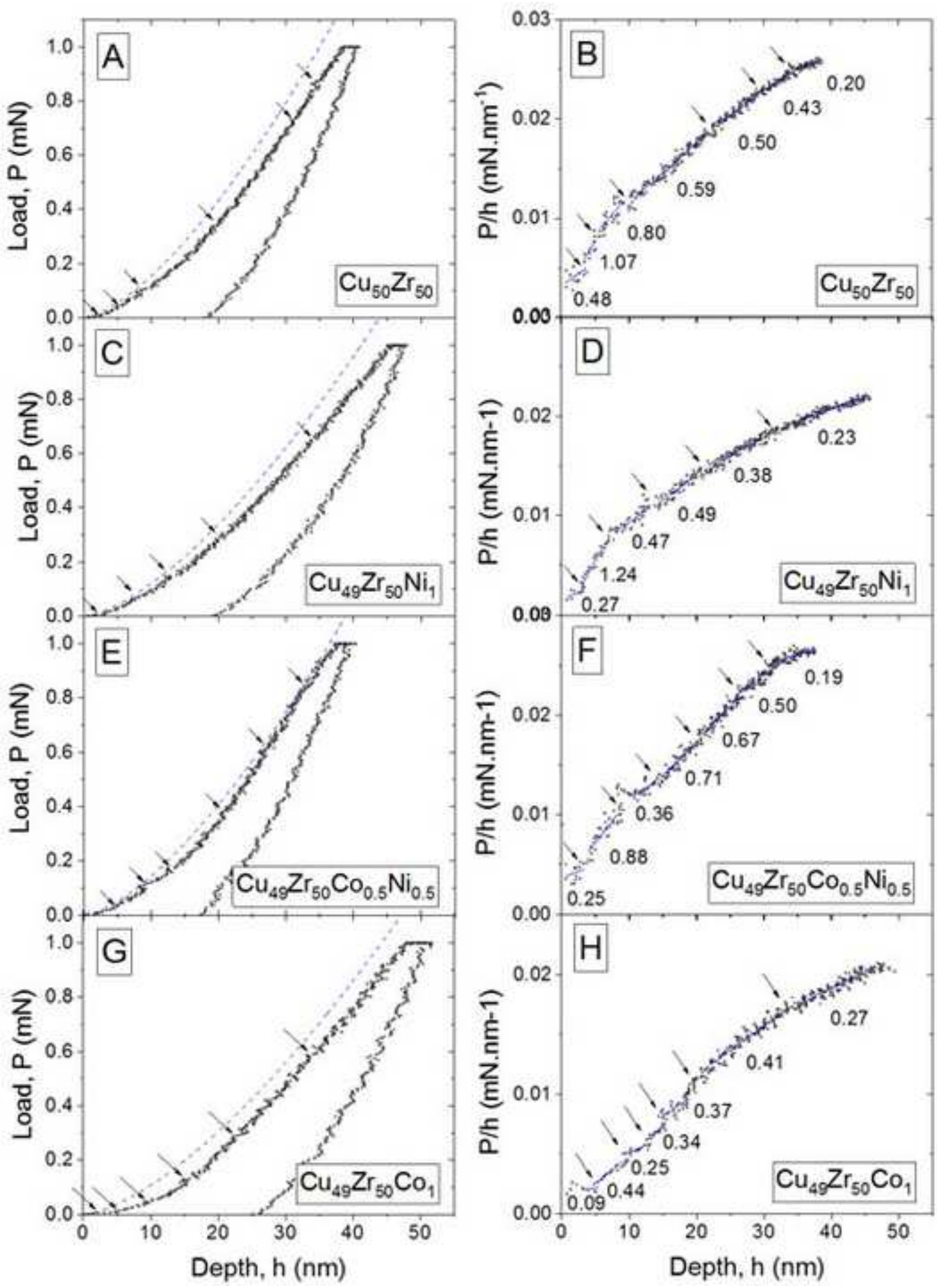

Figure
Click here to download high resolution image

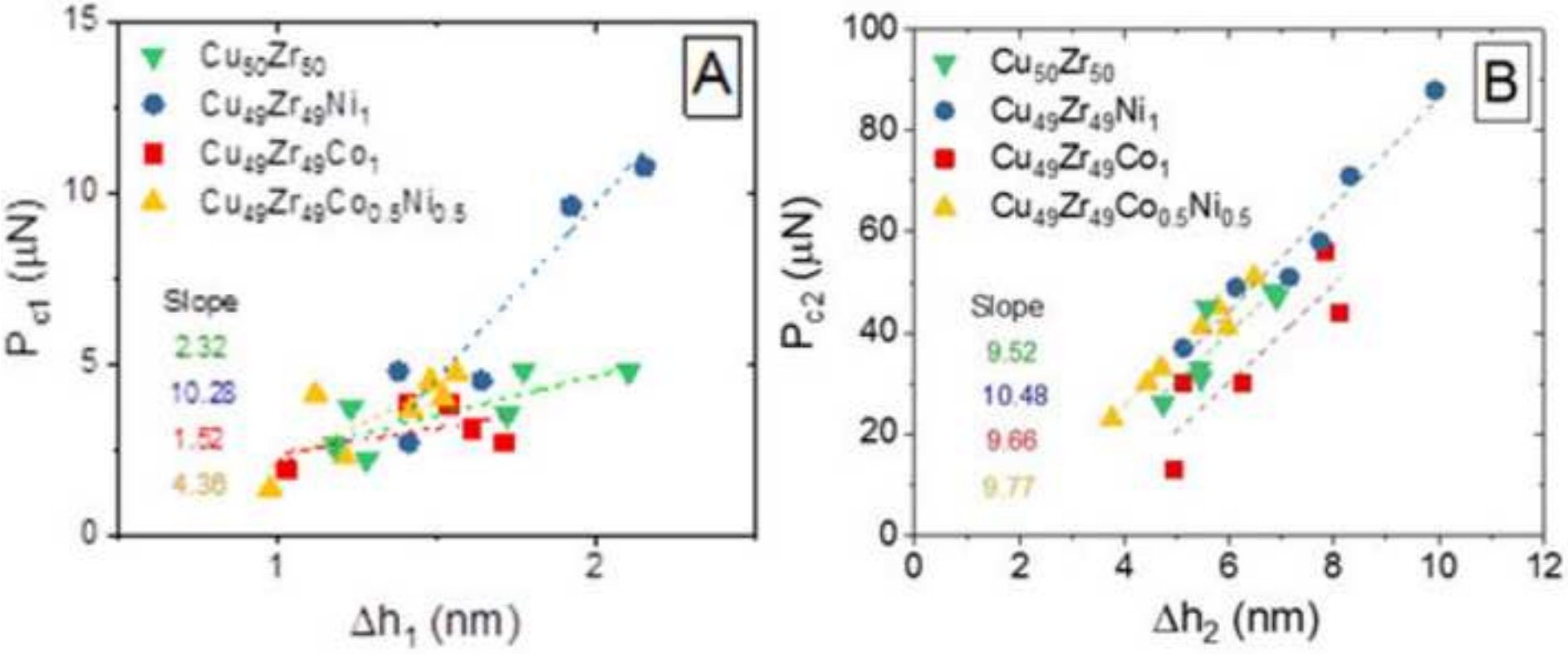

Figure
Click here to download high resolution image

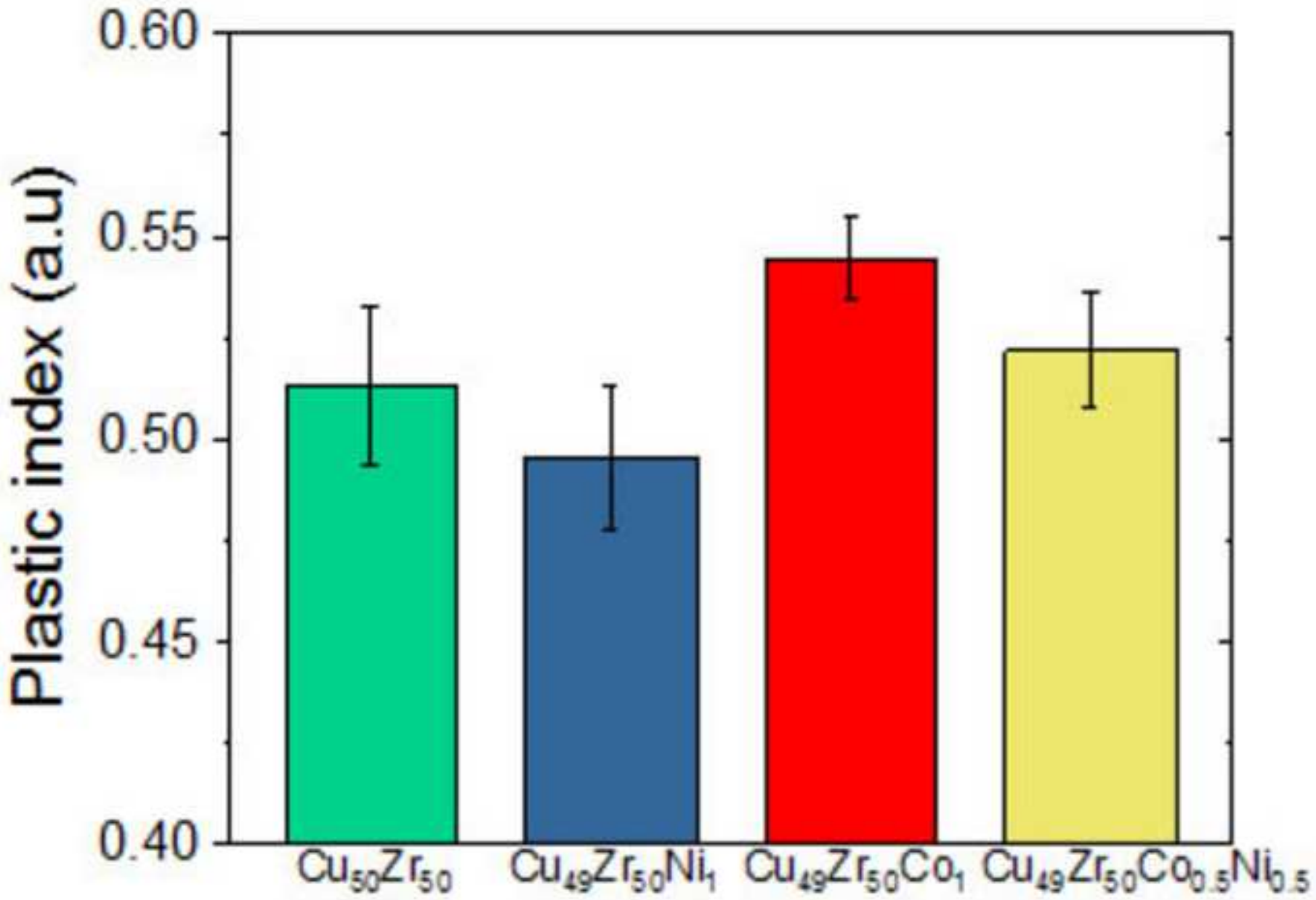

Figure
Click here to download high resolution image

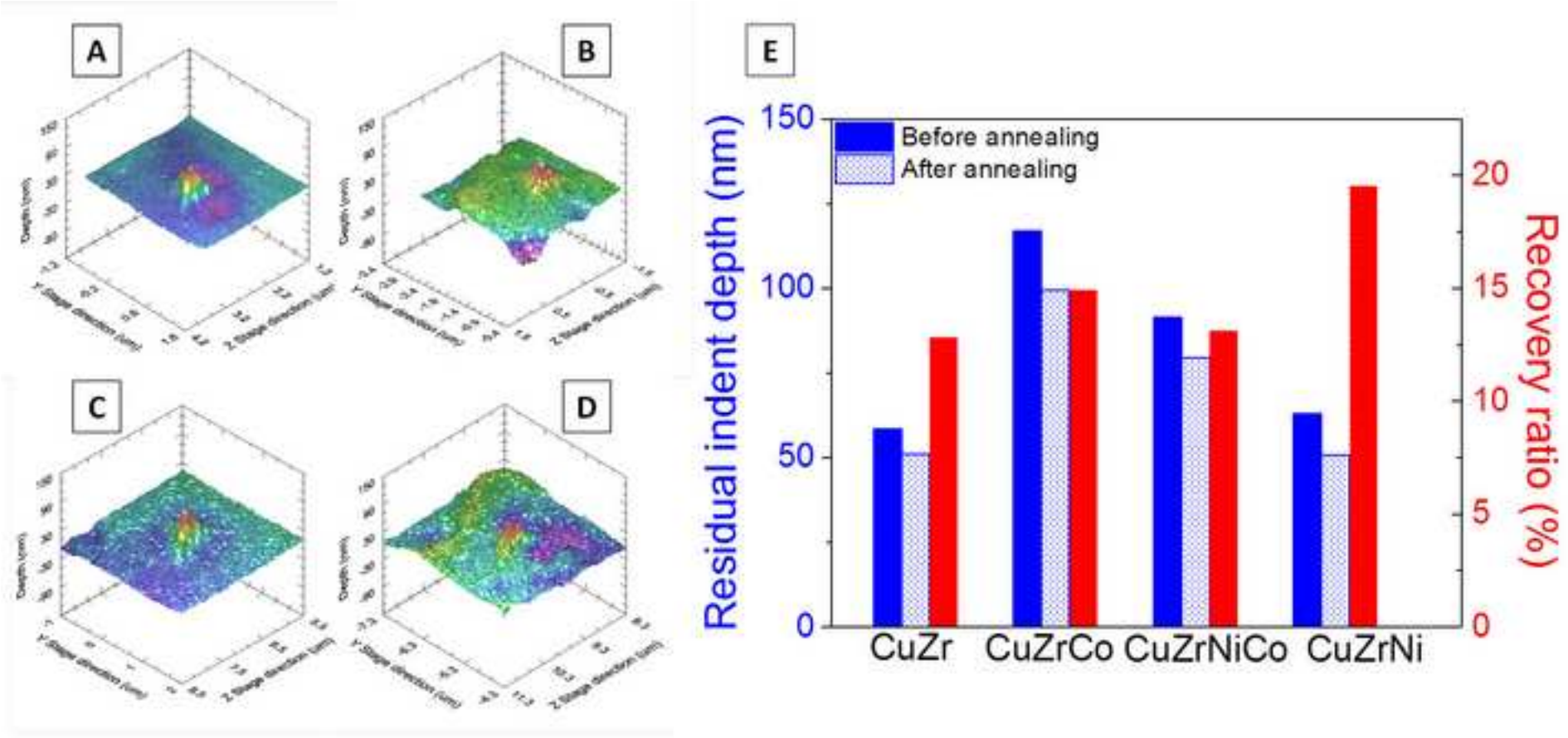

Figure

Click here to download high resolution image

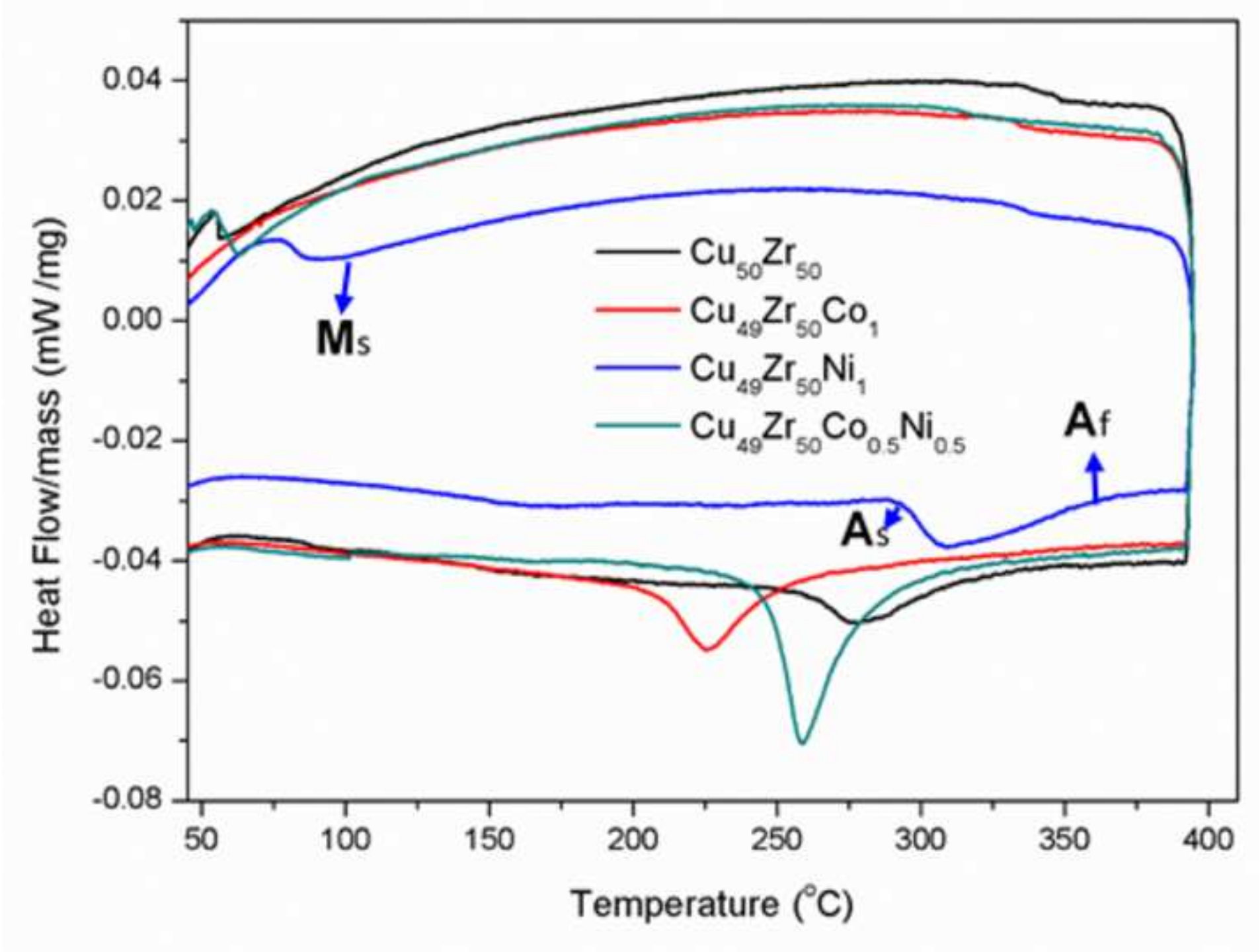

Figure
Click here to download high resolution image